sensors, equally based on cooled and uncooled devices, have promises of high thermal resolution and accuracy. However, the remarkable spread of IR technology, together with the reduction in the size of IR sensors, directed the designers and companies to invent even mobile thermal cameras [6].

To overcome the restrictions of contact measuring devices, the IR thermography imaging has been used in multidisciplinary applications. Servais and Gerlach [7] developed a method to inspect the composite material of aircraft using an IR camera, where they use high sensitivity and digital signal processing to evaluate the aircraft edging condition. Sousa et al. [8] and Bagavathiappan et al. [9] presented the military applications of a thermal camera to detect unseen moving objects. Jaffery and Dubey [10] and Mclntoch [11], used IR camera images as an early defective warning strategy for electrical systems. In medical detection and diagnosis, Sousa et al. [12] and Joudi et al. [13], both used the IR camera once for the detection of the healthy condition of the human hand joints and the human cornea during laser eye surgery, respectively. Vardasca et al. [14] suggested a new connection between the IR camera images and machine learning, especially for biomedical applications.

Cast-iron has become an engineering material with a wide range of applications used in pipes, machines, automobiles, and many small and large industrial parts. The thermal properties of such material represent a critical point of selection and use, especially when we are affected by a range of temperatures. This is the principal reason why thermal properties are considered as a guideline for cast-iron applications [15]. Miha Pevec et al. [16] investigated the mechanical properties and low cycle fatigue (LCF) behavior of brake discs gray cast iron at room and elevated temperatures. Belhocine and Bouchetara [17] presented a numerical modeling in three dimensions to analyze the thermal behavior of the full and ventilated disc brake using code ANSYS 11. Mellouli et al. [18] presented a study on the thermal fatigue damages of four nodular cast irons which are formed by adding different elements. They had proposed to examine that, by the addition of different elements, had effect on the crack growth and oxidation, thermal cycle of cast iron specimen.

Nondestructive testing strategies are extensively utilized for the primary recognition of possible failure of a material, component, or system. These strategies do not modify or impair the object under examination and, intrinsically, deliver a respected device to increase protection while minimizing the related costs [19]. Infrared thermography or non–contact inspection has been extensively used in assessing the conditions of different types and parts of machinery [20]. To prevent major mechanical failures and keep follow up conditions for different parts of machines like the rotor shaft, stator, bearings, and so on, monitoring thermography is a powerful suggestion [21].

Conversely, these tests are in generally having an initial assigned schedule and don not describe the performance of the components during the working load. On the other hand, the online healthy tests or inspections, which are mostly done during the operational workload, feedback the examiner with real potential safety and danger level, preventing finally the hazard that may cause sudden damage and fail to serve [22].

In the present study, IR cameras were used to measure the cooling process of a hot square cross-sectional shaft by measuring the temperature of the four faces from nine different projections. These projections have an apartment of 45° angle. Each image carries a detail of approximately 26 × 44 points of measurement. These values gave an indication of the material thermal behavior, and the fluctuation in some points inside the whole matrix of measurements looks to be an indication for local material deficiency.

MODELING OF IR THERMOGRAPHY

Radiation Analysis

Everything at a temperature greater than the absolute zero (–273° C), radiates heat as an energy called infrared energy. This energy varies from one body to another depending on the type of material and its temperature. The radiated energy is classified into three parts: absorption, transmission, and reflection [23]. The absorptivity, transmissivity, and reflectivity are the three fractions of energy from the total radiant energy of any body. The spectral absorptance (α_λ), the spectral transmittance (τ_λ), and spectral reflectance (ρ_λ), which are the ratio of the spectral radiant absorbed, transmitted, and reflected power by the surface [24]. The wavelength (λ) here is the independent variable that affects directly the three ratios, the sum of which must be unity, as described by Kirchoff's law in equation (1):

$$\alpha_\lambda + \tau_\lambda + \rho_\lambda = 1 \tag{1}$$

Thermal cameras are considered most of the materials as nontransparent materials (black body) so that, the transmission factor can be neglected and consider it equal to zero ($\tau_\lambda = 0$). Hence eq. (1) is simplified to eq. (2).

$$\alpha_\lambda + \rho_\lambda = 1 \tag{2}$$

Opaque bodies and blackbodies are not transmitted and only absorbed energy bodies, respectively, are two special cases of radiant energy body.

Plank's law, used to calculate the blackbody radiation ($W_{\lambda b}$) as in equation (3):

$$W_{\lambda b} = \frac{C_1 \lambda^{-5}}{e^{\frac{C_2}{\lambda T}} - 1} \tag{3}$$

where, $W_{\lambda b}$ is the power per unit area per unit length, C_1 and C_2 are constants, λ is the wavelength, and T is the temperature.

The emitted radiation and the temperature are related reversely, higher temperature object emitted a shorter wavelength. Wein's law is used to find the maximum radiation intensity, as in equation (4):

$$\lambda_{peak} = \frac{0.0029}{T} \tag{4}$$

To obtain the total radiation intensity of a blackbody using the Stefan – Boltzmann equation:

$$W_b = \sigma.T^4 \tag{5}$$

While the emissivity of the real body is not constant or depends on the wavelength, the Stefan – Boltzmann equation this time will be:

$$W_b = \varepsilon.\sigma.T^4 \tag{6}$$

where σ is a Boltzmann constant and ε is the emissivity of the real body.

Temperature Measurement Using IR Camera

The IR camera reads the IR thermal energy emitted from the object and converts this energy to the equivalent temperature value. The surrounding radiation energy and the other objects bother the read values and must be compensated to reach the optimum measurement.

Consider (W_{tot}) as the total radiation energy received, which represents three sources: (E_{obj}) the required object to be measured, (E_{refl}) the surrounding reflection, and (E_{atm}) atmospherically energy. Equation (7) describes the relationship between the energies (see Fig. 1):

$$W_{tot} = E_{obj} + E_{refl} + E_{atm} \tag{7}$$

To find out the mean required temperature, which was measured by the IR camera for each surface (local positions), substitute equation (6) for each term in equation (7) and rearranging it to get the following equation:

$$T_{obj} = \sqrt[4]{\frac{W_{tot} - \left(-\varepsilon_{obj}\right).T_{atm}.\sigma.\left(T_{refl}\right)^4 - \left(1-T_{atm}\right).\sigma.\left(T_{atm}\right)^4}{\varepsilon_{obj}.T_{atm}.\sigma}} \tag{8}$$

T_{obj} is the mean estimated value for the radiated surface. This value is used as a reference for the measurements along the surface done an IR camera. Equation (8) can be solved after defining the emissivity's, transmittance, and temperatures of the atmosphere and reference. The emissivity's and transmittance values lead to different types of media used in the IR camera according to the useful range of detection.

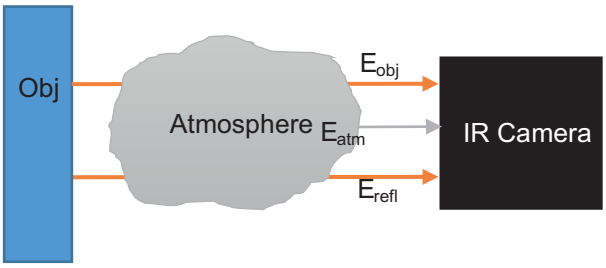

Figure 1. Three components of total radiation.

The T_{atm} is commonly assumed close to one, while the T_{amb} is measured by a thermometer. Instead, ε_{obj} and T_{refl} have a very high influence on the temperature measurement.

NON-INVASIVE OR NON-DESTRUCTIVE TESTING

IR thermography has been used at the last few years intensively in the non-destructive measurements, by interpreting the temperature of the measured object surface. The temperature distribution appears upon the surface of the measured object is an important indication for the internal structure behavior toward the thermal energy. This is the main idea behind measuring the local temperature on the surface of the object, which reflects the defects of the material. The possibility of detecting such faults on the internal structure of materials is increased when using data processing techniques, especially with weak surface gradient temperatures.

In general, there are passive or active approaches used in the nondestructive tests of materials. The difference between the two approaches that the passive the inspected body at a different temperature, while the active test done on the body at the same time where an external active motivation was applied to the same body. The objective here is to create a thermal gradient and investigate the faults, defects, or structural problems. Thermography always deals with the propagated thermal waves by conduction, convection, or radiation, either from the surface to the surface or from the heat generation position to the surface through the tested object. The normal temperature distribution is an indication for the internal structure regular behaves and vice versa. In the present work, we introduce an active approach test by heating a shaft with a square cross-sectional area and measuring the thermal energy dissipated from it by describing the temperature in the nine topographical positions.

The test here is done during the cooling stage of the shaft, where the temperature started to decrease with time during image capture. Each image has a background or base temperature and projection side that we can identify the deficiencies during cooling from different sides of the material tested.

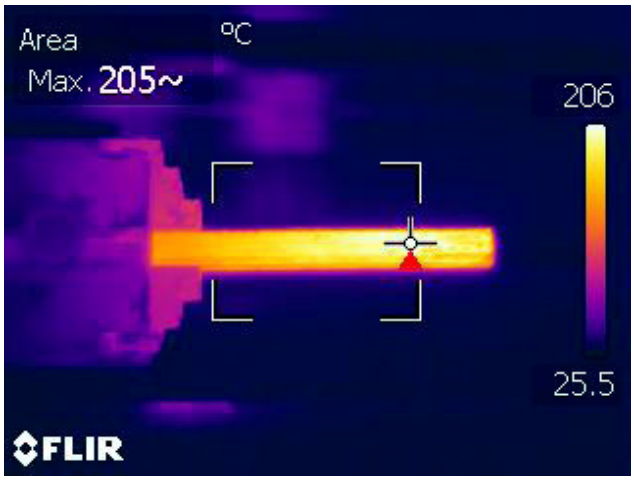

Figure 4. Capture image of the 1st plane of angle 0° with the position and size of the discussed area of interest.

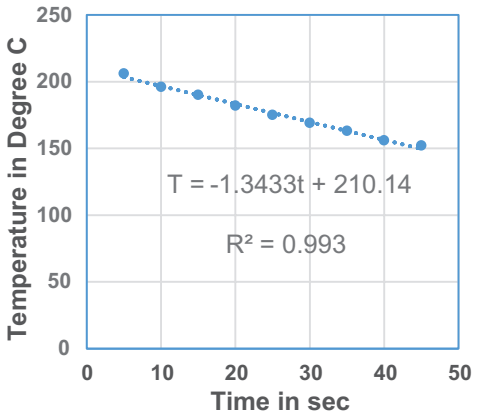

Figure 5. Heat dissipation during the measurement of projections.

7. Total nine images of the specimen have been captured. Out of nine images, five represented direct faces and four represented the mix of two faces.

The final projection from each part projection that will be discussed in the result is the central part of the specimen with a length of 200mm (10mm to each side from the center of the specimen), with a width of 13mm (1mm added from each side, above and below). This inspected area has a matrix size of (26 x 44) which represents approximately a cell of (0.5mm by 0.5mm) per each line from the heat map.

RESULTS

The collected results here are according to the practical inspection of the tested sample. No previous studies used such settings or conditions that could be used to validate the results. Finally, the results were manipulated and compared with each section and slice with each other.

Cooling Rate

Finally, nine projections were recorded from different angles as mentioned above. Each projection has a different maximum temperature; Fig. 5 shows the temperature variation (cooling rate) during the nine steps. The linear interpolation for the nine values to predict the maximum temperature during the cooling back with the following relation:

$$T = -1.3433t + 210.14 \quad (9)$$

where, T is the temperature in °C and t is the time in seconds. With a root mean square error (R^2) is equal to 0.9936. The heat rate of dissipation can be calculated by differentiation of equation (9), then $\frac{dT}{dt} = 1.3433$ which means a drop of about 1.34° C per second.

Rate of changes in temperature is an indication for a local position defect. This defect will be confirmed more precisely in the multi projection temperature.

Projection Analysis

Figure 6 shows the procedure, and the application programs need to read and draw the projections. Starting from the left, the image captured first using the IR camera, and then transferred to the computer where the analysis program was used to read the raw data. The data exported from the previous step in the csv file form that could be imported by Python 3.7 as an analysis program. Finally, the module matplotlib 3.1.2, as an interpretation tool for the heat map.

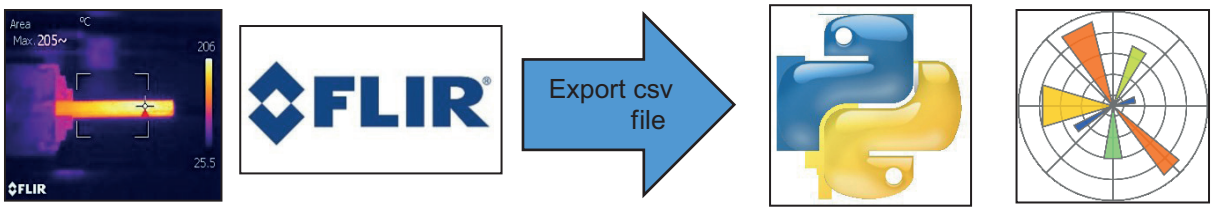

Figure 6. Applications used to create and study each projection.

Direct Projections

Figure 7 shows the heat map for the first projection classified as a matrix of (44 x 26) (as mentioned in the previous section). The matrix size here represents the real resolution of the IR image received from the IR camera. The regions of interest (ROI) for the map below are classified into the following regions according to the temperature variation, these regions are:

a. Environmental temperature (S_01, S_02 from the upper surface and S_25, S_26 from the lower surface) with mean values of 30.8° C, 37.3° C, 36.4° C and 32.0° C, respectively.
b. Convection film layer temperature (S_03, S_04 for the upper surface and S_21, S_22, S_23, S_24 for the lower surface) with mean values of 96.3° C, 169.2° C, 158.8° C, 154.7° C, 122.2° C and 54.2° C, respectively.
c. Material temperature (from S_05 to S_20) with an average of mean values of 186.3° C.

Figure 8 shows the variation in the mean values for the above three regions along the nine projections. The

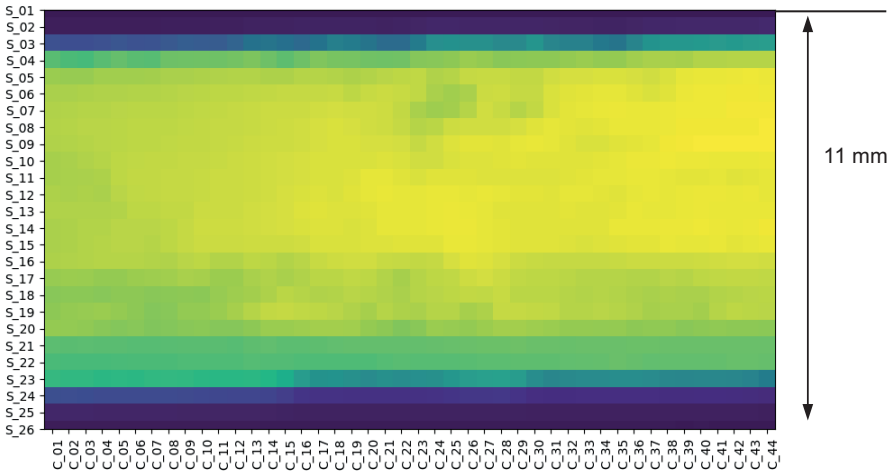

Figure 7. First face heat map.

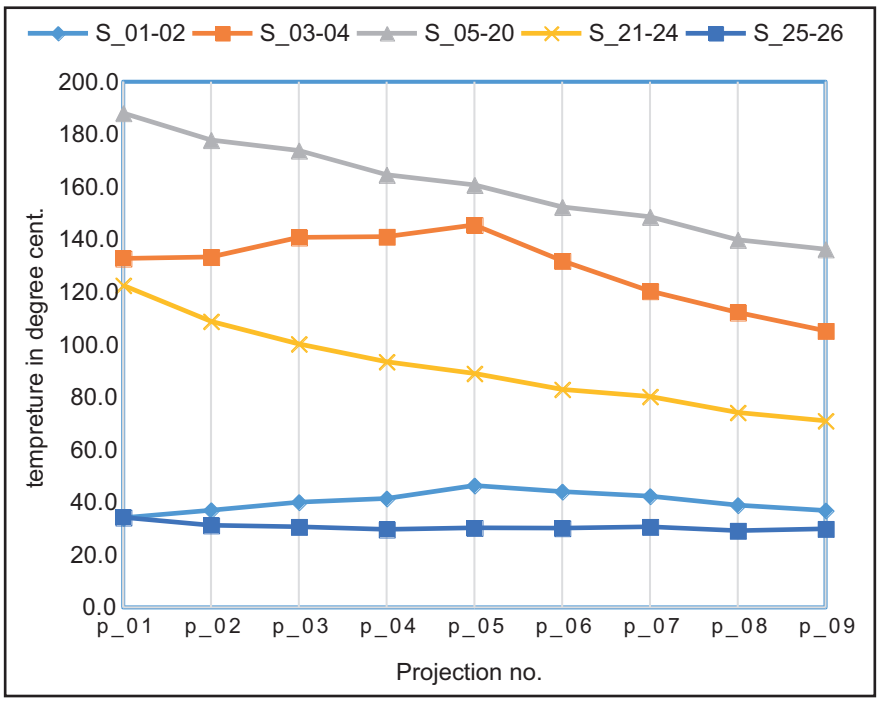

Figure 8. Average temperature variations for the three regions for nine projections.

fluctuation in the central and the two environmental regions decreased regularly while the other two film layers increased in the first phase and then decreased like the other layers.

Figure 9 shows the radar variation in the mean temperature for the material temperature layer or the nine projections. It is possible here to predict the number of projections required to reach a specific temperature for any surface of the material.

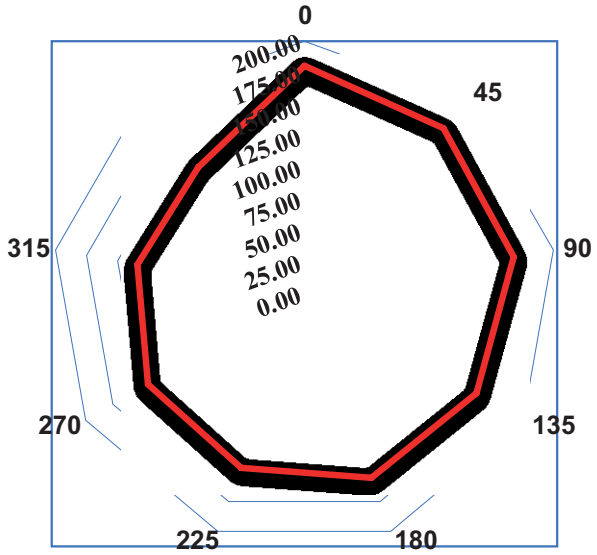

Figure 9. Average radar temperature variations for the material region for nine projections.

Oblique Projections

Figure 10 shows the heat map for the second projection classified to a matrix of (44 x 26). The matrix size here represents the real resolution of the IR image received from the IR camera. The regions of interest (ROI) for the map below are classified into the following regions according to the temperature variation, these regions are:

a. Environmental temperature (S_01, S_02 from the upper surface and S_25, S_26 from the lower surface) with mean values of 31.0° C, 42.8° C, 36.7° C and 32.0° C, respectively.
b. Convection film layer temperature (S_03, S_04 for the upper surface and S_21, S_22, S_23, S_24 for the lower surface) with mean values of 83.5° C, 161.7° C, 161.4° C, 146.3° C, 122.7° C and 55.4° C, respectively.
c. Material temperature (from S_05 to S_20) with an average of mean values of 178.2° C.

For the oblique faces, the distance of their center is not equal to the distances of the two other boarders. Although this difference in distance is presented, it does not effected the measured temperature. This is related to the fact that the radiated energy diffused in every direction and the small dimension size of the measured object that reflected the neglected amount of differences.

Slice Analysis

The vertical section through the heat maps for different projections is called the slices. The behavior of the temperature per element position is considered as a reflex from the material to diffuse the heat energy outside the heated

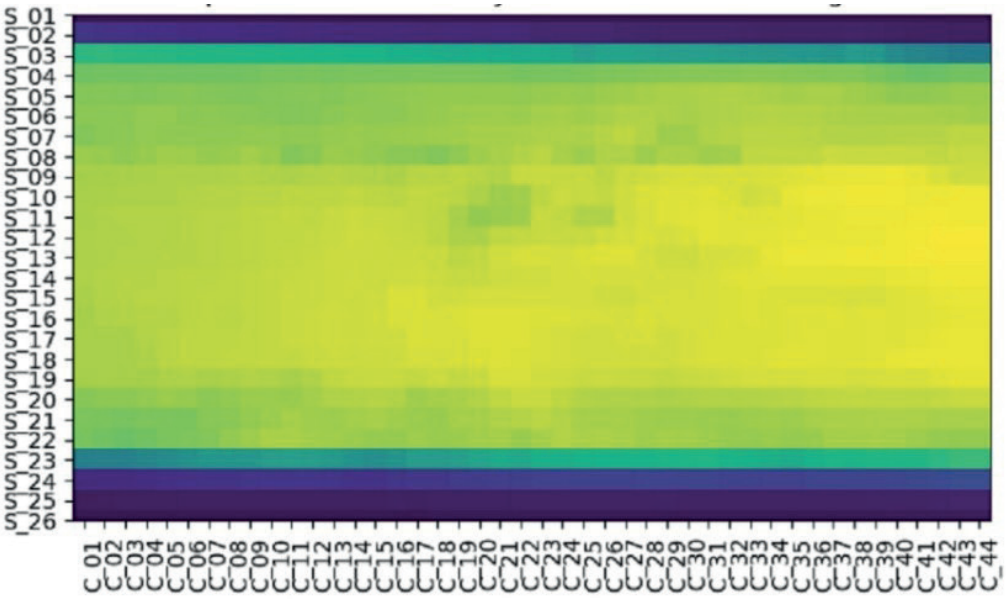

Figure 10. Second oblique face heat map.

specimen. Figure 11 shows the 44 slices mean temperature for the different nine projections with their linear interpolation functions. Each line has its own linear fitting equation and square root mean error, with details given in Table 2.

DISCUSSION

The inspection of material was done by adding an external energy or by measuring the dissipated energy, as this was an important procedure in the experimental study. This is done here by heating and then measuring the cooling rate from different faces at different projection angles of the specimen. The analysis of the projections of heat maps collected from an IR camera leads us to understand the variation in different local positions and regions of the specimen, starting from the environmental layer reaching the main material once. These local positions and regions are defined here by slice numbers S-code for horizontal and C-code for vertical. Layer C_22 indicates two times in two different projections (2 and 9) their significant differences in temperature with respect to the real measured and interpolated values. Also, Layer C_28 shows the highest temperature difference about 2.51° C in projection 4 compared to all the other layers.

By calculating the error between the interpolation functions and the real measured values per each projection, the following slices per projection have the maximum difference in temperature, as in Table 3.

The above differences in temperature per projection may initially indicate local changes in the behavior of the

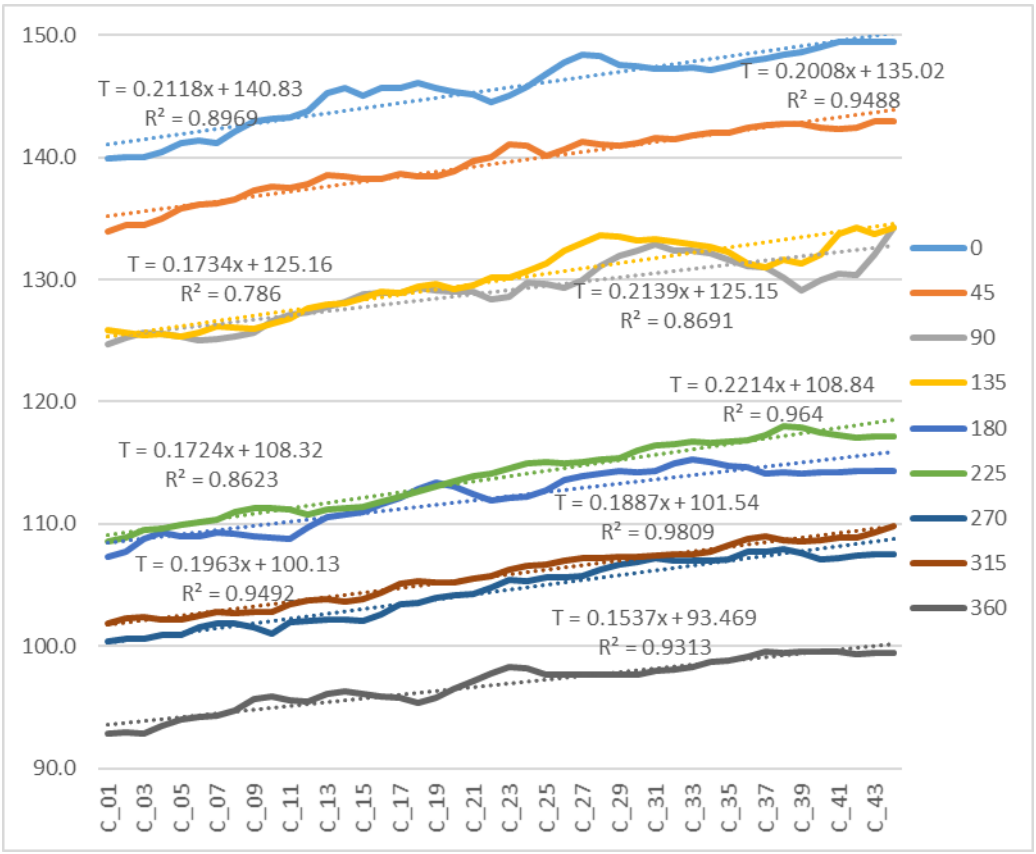

Figure 11. The 44 slice temperatures for nine different projections of with their linear interpolation functions.

Table 2. Coefficients of linear polynomial for the nine projections

Projection No.	1	2	3	4	5	6	7	8	9
M	0.2118	0.2008	0.1734	0.2139	0.1724	0.2214	0.1963	0.1887	0.1537
B	140.83	135.02	125.16	125.15	108.32	108.84	100.13	101.54	93.469
Root square error	0.8969	0.9488	0.786	0.8691	0.8623	0.964	0.9492	0.9809	0.9313
y (Temperature °C) = M*X (slice number) + B									

Table 3. Slice number, projection, and the difference in temperature between the linear interpolations function and real measured values

Slice	Projection(s)	Mean actual measured T in °C	Interpolated T in °C	Difference in °C
C_19	5	163.51	165.32	1.81
C_22	2, 9	182.48, 140.40	181.48, 139.12	1.41, 1.28
C_27	1	181.69	183.56	1.87
C_28	4	166.41	163.9	2.51

material that practically relative to the local deficiency that needs a mechanical inspection procedure to reach the final decision.

CONCLUSIONS

Adding heat energy to measure the cooling process from different projections is a good nondestructive test that will help and guide the standard mechanical inspection procedure. Specifying projection and slice position will increase the percentage of correctness of the local and global assessment for test samples. Taking the projections around the measured part is the main limitation for the size of the object, and also the irregularities in the external shape will affect the number of required projections for the analysis. But still we have good promise to assist the mechanical parts online non – invasively with no cost effect and easy be manipulation and analysis through the new techniques of image processing to be considered as an early warning technique.

NOMENCLATURE

C	Local slices
C_1,C_2	Constants
CCW	Counter clockwise
E_{obj}	Object energy
E_{refl}	Reflection energy
E_{atm}	Atmospherically energy
IR	Infrared
ROI	Regions of interest
R^2	Root mean square error
S	Local surface
T	Temperature
t	Time
W_{tot}	Total radiation energy

Greek symbols

α_λ	Spectral absorptance
τ_λ	Spectral transmittance
ρ_λ	Spectral reflectance
λ	Wavelength
$W_{\lambda b}$	Blackbody radiation
σ	Boltzmann constant
ε	Emissivity

AUTHORSHIP CONTRIBUTIONS

Authors equally contributed to this work.

DATA AVAILABILITY STATEMENT

The authors confirm that the data that supports the findings of this study are available within the article. Raw data that support the finding of this study are available from the corresponding author, upon reasonable request.

CONFLICT OF INTEREST

The author declared no potential conflicts of interest with respect to the research, authorship, and/or publication of this article.

ETHICS

There are no ethical issues with the publication of this manuscript.

REFERENCES

[1] Kastberger G, Stachl R. Infrared imaging technologies and biological applications. Behav Res Meth Instrum Comput 2003;35:429–439. [CrossRef]

[2] Breglio G, Irace A, Maresca L, Riccio M, Romano G, Spirito P. Infrared Thermography applied to power electron devices investigation. FU Elec Energ 2015;28:205–212. [CrossRef]

[3] Usamentiaga R, Venegas P, Guerediaga J, Vega L, Molleda J, Bulnes FG. Infrared thermography for temperature measurement and non-destructive testing. Sensors (Switzerland) 2014;14:12305–12348. [CrossRef]

[4] Cardone D, Merla A. New frontiers for applications of thermal infrared imaging devices: computational psycho-physiology in the neurosciences. Sensors (Switzerland) 2017;17:1041–1242. [CrossRef]

[5] Gade R, Moeslund TB. Thermal cameras and applications: a survey. Mach Vis Appl 2014;25:245–262. [CrossRef]

[6] Rogaliski A. Infrared detectors for the future. Acta Phys Pol A 2009;116:389–406. [CrossRef]

[7] Servais P, Gerlach N. Development of a NDT method using thermography for composite material inspection on aircraft using military thermal imager, Proc. 5th Int. Workshop, Advances in Signal Processing for Non Destructive Evaluation of Materials Québec City (Canada), 2005, p. 2–4.

[8] Akula A, Ghosh R, Sardana HK. Thermal imaging and its application in defense systems. AIP Conf Proceed 2011;1391:333–335. [CrossRef]

[9] Bagavathiappan S, Lahiri BB, Saravanan T, Philip J, Jayakumar T. Infrared thermography for condition monitoring A review. Infrared Phys Technol 2014;60:35–55. [CrossRef]

[10] Jaffery ZA, Dubey AK. Design of early fault detection technique for electrical assets using infrared thermograms. Int J Electr Power Energy Syst 2014;63:753–759. [CrossRef]

[11] Mclntosh GB. Condition assessment of electrical connections utilizing infrared thermography. Quantit Infrared Thermogr 2014:1–10. [CrossRef]

[12] Sousa E, Vardasca R, Teixeira S, Seixas A, Mendes J, Costa-Ferreira A. A review on the application of medical infrared thermal imaging in hands. Infrared Phys Technol 2017;85:315–323. [CrossRef]

[13] Joudi KA, Somer MN, Nebras HG. Thermal topographical rings as a new tool for laser eye surgery. J Biomed Eng Technol 2017;5:1–5.

[14] Vardasca R, Magalhaes C, Mendes J. Biomedical applications of infrared thermal imaging: current state of machine learning classification. Proceedings 2019;27:46. [CrossRef]

[15] Guesser WL, Masiero I, Melleras E, Cabezas CS. Thermal conductivity of gray iron and compacted graphite iron used for cylinder heads. Rev Matér 2005;10:265–272.

[16] Pevec M, Oder G, Potrc I, Šraml M. Elevated temperature low cycle fatigue of grey cast iron for automotive brake discs, Eng Fail Anal 2014;42:221–230. [CrossRef]

[17] Belhocine A, Bouchetara M. Thermal analysis of a solid brake disc. Appl Therm Eng 2012;32:59–67. [CrossRef]

[18] Mellouli D, Haddar N, Köster A, Marie-Louise Toure A. Thermal fatigue of cast irons for automotive application. Mater Design 2011;32:1508–1514. [CrossRef]

[19] Stankovicová Z, Dekyš V, Novy F, Novák P. Nondestructive testing of metal parts by using infrared camera. Procedia Eng 2017;177:562–567. [CrossRef]

[20] Gupta VK, Varde PV, Kankar PK, Joshi N. Reliability and Risk Assessment in Engineering, Proceedings of INCRS 2018, Singapore: Springer Nature Pte. Ltd.; 2020. [CrossRef]

[21] Jayaswal P, Wadhwani AK, Mulchandani KB. Machine Fault Signature Analysis. Int J Rotating Mach 2008:583982. [CrossRef]

[22] Bagavathiappab S, Lahiri BG, Saravanan T, John P, Jayakumar T. Infrared thermography for condition monitoring – a review. Infrared Phys Technol 2013;60:35–55. [CrossRef]

[23] Vollmer M, Mollmann KP. Infrared Thermal Imaging. Berlin: WILEY-VCH; 2011. [CrossRef]

[24] Howell JR, Siegel R, Menguc MP. Thermal Radiation Heat Transfer. 5th ed. New York: Taylor and Francis; 2010. [CrossRef]